In situ stress measurements of metal oxide thin films

5

A. Fluri, C.W. Schneider, D. Pergolesi
Paul Scherrer Institut, Villigen, Switzerland

5.1 Materials engineering in heteroepitaxial thin films

Physical properties of materials can be significantly altered without changing their composition thereby enhancing or inhibiting properties or even invoking new functionalities. These changes can be enforced through lattice distortions (strain), microstructural/morphological changes (e.g., grain size, porosity), or by creating an interface between two materials which exhibits properties that none of the parent compounds have. Examples of interface effects include magnetic interfaces in the $YBa_2Cu_3O_7/La_{2/3}Ca_{1/3}MnO_3$ system [1,2], or the electrically conducting interface between epitaxially grown $LaAlO_3$ and $SrTiO_3$ with the emergence of superconductivity, magnetism, and strong spin–orbit coupling at such interfaces [3–7]. Likewise amorphous $LaAlO_3$ grown on $SrTiO_3$ gives rise to conducting interfaces and due to a very high mobility, a quantum hall effect can be observed [8,9]. It is interesting to note that for both kinds of conducting interfaces their structural integrity needs to be preserved. For the epitaxially grown films, oxygen vacancies lead to an excess conductivity [10] whereas structural defects such as dislocations suppress the conductivity [11,12]. For the amorphous $LaAlO_3$ layer, charge transfer-induced modulation-doping with one epitaxially grown monolayer of $La_{1-x}Sr_xMnO_3$ ($x=1/8$, $1/3$) grown on TiO_2-terminated $SrTiO_3$ enhances the electronic conductivity up to 100 times [13].

Lattice distortions in a crystal change the bond lengths and hence the electron density, which can strongly influence the physicochemical characteristics thereof. Strain affects materials in many different ways like the electronic bandgap [14], the behavior of correlated systems [15], thermal conductivity [16], multiferroicity [17,18], catalytic properties [19], and charge transport [20–23]. The tuning of material properties via lattice distortions is referred to as strain engineering. Significant strain effects are reported for catalytic properties of surfaces [19,24–31]. For state-of-the-art electrocatalysts, Pt-based materials are the preferred catalysts; however they face the problem of poor electrochemical oxygen reduction kinetics. By tuning, e.g., the strain in epitaxially grown Pt films, the electrochemical surface properties of Pt can be significantly enhanced [31]. Other examples of strain engineering are the introduction of ferroelectricity at room temperature in $SrTiO_3$ thin films [32] or a significantly enhanced ferroelectric phase of $BaTiO_3$ [33]. Likewise, the multiferroic phase of coherently grown orthorhombic rare-earth manganites can be substantially changed by applying appropriate strain [34]. An example of the influence of lattice distortions

Metal Oxide-Based Thin Film Structures. https://doi.org/10.1016/B978-0-12-811166-6.00005-4
© 2018 Elsevier Inc. All rights reserved.

on charge transport is the reduction of the energy barrier for oxygen ion transport in Sm-doped ceria, a typical electrolyte material in solid-state electrolyte fuel cells [35].

Heteroepitaxial thin films, where strain arises due to a lattice mismatch of film and substrate, are ideal tools to investigate the influence of the strain on material properties. For a certain mismatch, the maximum strain can be theoretically achieved when the film adopts the lattice parameter of the substrate forming a coherent interface. However, the interface often contains defects which reduce or even fully relax the strain. The structural, morphological, and chemical characteristics of the interface are inherently connected to the strain in the thin film so that understanding the strain generation and relaxation is crucial not only for strain engineering but also for studying interface effects.

In this chapter, an epitaxial thin film with a cubic crystal structure is considered. The bulk lattice constant of the film, a_0, and the substrate, a_s, result in a lattice mismatch $f=(a_s-a_0)/a_0$. In thin films the strain is biaxial, meaning that it is applied equally along two in-plane directions while the third (out-of-plane) direction is free to adapt. With a and c denoting the in-plane and out-of-plane lattice constants, the biaxial in-plane strain $\varepsilon=(a-a_0)/a_0$ and the out-of-plane strain $\varepsilon_{zz}=(c-a_0)/a_0$ are related via the Poisson ratio ν as [36]

$$\varepsilon_{zz}=2v\varepsilon/(v-1) \tag{5.1}$$

The sign of the strain is defined as positive for tensile and negative for compressive. The force per unit area required to induce a strain ε is the stress $\sigma=\varepsilon E$, where E is the elastic modulus. For large values of the elastic modulus E the material is rigid and difficult to distort. In the case of biaxial strain in a cubic symmetry, $E=Y/(1-\nu)$ where Y is the Young's modulus [37].

A lattice mismatch $|f|\leq 1\%–2\%$ may typically be expected to be fully accommodated in a thin semiconductor film [37–40]. The case of perfect coupling (Fig. 5.1) between the film and the substrate in-plane crystal lattice is referred to as pseudomorphic growth; the interface is coherent with $a=a_s$ and $f=\varepsilon$. Due to imperfections in the crystal lattice, imperfections at the substrate/film interface, or due to the surface morphology of the film (roughness), the in-plane lattice constant of a film can partially adapt to the substrate, or even fully relax ($|\varepsilon|<|f|$). The strain in a film will relax

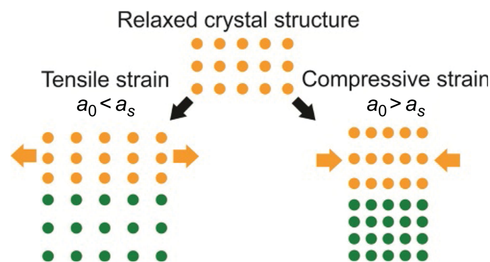

Fig. 5.1 Epitaxial strain developed during pseudomorphic growth. A material with a lattice constant a_0 of the relaxed crystal structure is grown on a substrate with a lattice constant a_s. For $a_0<a_s$ tensile strain develops (compressive out-of-plane) and for $a_0>a_s$ it is compressive (tensile out-of-plane). The forces required to induce the in-plane lattice distortion are indicated by *orange arrows*.

as a function of film thickness through the introduction of crystalline defects thereby reducing the elastic energy in the film.

To unambiguously correlate the physical properties of specific materials grown as thin films to different strain values, it is crucial that these films differ only with respect to strain, but not in composition or morphology, as these parameters also influence the lattice constant and hence the strain. Tuning the strain by using different growth conditions is therefore not an option since small change in growth conditions can significantly change the composition. This also includes oxygen vacancies. For oxide thin film growth, this has been studied, e.g., for $SrTiO_3$ thin films grown by molecular beam epitaxy (MBE) [41] and pulsed laser deposition (PLD) [42] similar a range of different materials deposited by PLD [43–46]. Keeping growth parameters constant, different strain values are obtained by using substrates with different lattice constants. If the characterization of the material property in question restricts the substrate choice, e.g., concerning chemical interaction, electrical or optical properties of the substrate, one can make use of different degrees of strain relaxation of the film that may be achieved for different thicknesses. In any case, the question whether the observed effect on the material property arises from strain or is due to interface effects has to be answered. Hence the in situ observation of the stress generation and evolution during the film growth provides highly valuable insights into these mechanisms that cannot be gained by ex situ analysis.

5.2 Strain relaxation in epitaxial films: An overview of established principles and models

Several models have been developed for the strain relaxation with a particular emphasis on semiconductor epitaxy. Various relaxation routes have been identified and discussed. Among them are crack formation, interdiffusion, surface roughening, and, most prevalently, the introduction of a dislocation network at the interface. The most relevant theoretical models for epitaxial thin films are summarized in the following. More detailed information can be found in Refs. [37–40,47,48].

At first, a strained pseudomorphic thin film with a layer-by-layer growth mode is assumed, i.e., an atomically flat surface. Since a perfect crystal structure is the minimum energy configuration, the formation of a crystalline defect which can reduce the strain comes at an energy cost. As the film thickness increases, so does the elastic energy accumulated in the film until it becomes energetically favorable to introduce crystal defects to release some of the elastic strain through plastic relaxation. Typically, theoretical models define a critical thickness, h_C, above which relaxation mechanisms are energetically favorable [39].

In 1949 Frank and van der Merwe [49] established that one perfect monolayer may accommodate up to 9% lattice mismatch. Above this threshold it is energetically favorable to form misfit dislocations. The theoretical model for strain relaxation by Matthews, Mader and Light (1970) is based on Frank and van der Merwe's calculations [50]. They considered threading dislocations that exist in the substrate continue into the film. When the threading dislocations glide through the film, more interface

misfit dislocations are created and the film relaxes gradually [40] (see Fig. 5.2). The dislocation lines shown in Fig. 5.2 are not necessarily straight but can also bend.

The periodic crystal lattice constitutes a periodic potential barrier which the dislocation lines have to overcome in order to move through the crystal (lattice friction). This leads to a model involving activation energy. The periodic energy barrier can be overcome by means of elastic (strain) or thermal energy [38]. As crystal defects contain more energy than a perfect crystal, it is energetically favorable for dislocation lines to move to the nearest sample edge. This can be seen as a configurational force acting on a dislocation line which is derived from the energy needed to form a dislocation at a certain distance from the sample edge [50]. As a consequence, a critical thickness fulfilling

$$h_C = \left(b\frac{1-\nu\cos^2\theta}{8\pi f(1+\nu)\cos\lambda} \right) \ln\left(\frac{h}{b}\right) \tag{5.2}$$

is defined, where the Burger's vector b and the angles λ and θ describe the dislocation geometry. For a film of a thickness $h \leq h_C$ the film is fully strained ($\varepsilon = f$) and for $h > h_c$ the strain relaxation as a function of time t is described by

$$\epsilon(t) = f - \beta(1 - e^{-\alpha t}) \tag{5.3}$$

with $\beta = f - \left(b\frac{1-\nu\cos^2\theta}{8\pi h(t)(1+\nu)\cos\lambda} \right) \ln\left(\frac{h(t)}{b}\right)$ and $\alpha = \frac{2Gb^3\rho(1+\nu)\cos\theta\cos^2\lambda D_0 \exp\left(-\frac{U}{k_BT}\right)}{(1-\nu)k_BT}$; G is the shear modulus, ρ the number of dislocation lines per area, k_B the Boltzmann constant, *and* D_0e^{-U/k_BT} is the diffusion coefficient of the dislocation with an activation energy U at a temperature T.

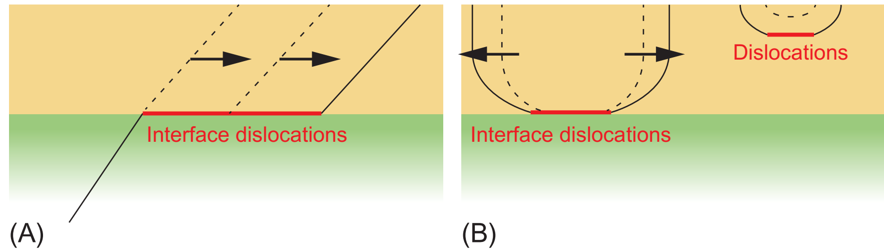

Fig. 5.2 Sketch of strain relaxation mechanisms. (A) Sketch of a threading dislocation that continues from the substrate into the film. If the dislocation line in the film moves, misfit dislocations are created interface *(red)*. (B) Sketch of dislocation half-loops that nucleate at the interface or on the surface of the growing film. Misfit dislocations parallel to the interface are indicated in *red*.

Another theoretical model based on Frank and van der Merwe's calculations and probably the most famous model for strain relaxation was introduced by Matthews and Blakeslee[51]. The force balance of the force exerted by the misfit strain and the tension in the dislocation line (i.e., crystallographic constraints keeping the dislocation in place) is considered. As long as the force exerted by the misfit strain is smaller, the film is fully strained. If the forces are equal, the Matthews-Blakeslee criterion for the critical thickness

$$h_C = \frac{b}{2\pi f} \frac{1-\nu \cos^2\gamma}{(1+\nu)\cos\eta} \left(\ln\left(\frac{h_C}{b}\right) + 1 \right) \tag{5.4}$$

is fulfilled, with the Burger's vector b and the angles γ and η describing the introduced dislocation and ν being the Poisson ratio of the film. Assuming equilibrium and the absence of kinetic barriers to the nucleation or to the glide of dislocations, the film relaxes above the critical thickness such that at each thickness h the strain is equal to the misfit that would yield $h_C = h$ in formula (5.4). The thickness dependence of the strain is given by

$$\epsilon(h) = \frac{b}{2\pi h} \frac{1-\nu \cos^2\alpha}{(1+\nu)\cos\lambda} \left(\ln\left(\frac{h}{b}\right) + 1 \right) \tag{5.5}$$

In other words, every increase in thickness implies an increase in the total elastic energy, which immediately makes a further relaxation energetically favorable. As a consequence, the total elastic energy will remain below a certain threshold during the growth. This model is very similar to the Matthews, Mader and Light model for $\alpha t \gg 1$, that is if there is no lattice friction [38,40]. The Matthews and Blakeslee model for the critical thickness applies, e.g., to the Ge_xSi_{1-x}/Si system at high (900°C) temperatures [52]. At lower temperatures (≤750°C), the critical thickness is larger than predicted by this equilibrium theory suggesting the presence of an energy barrier that suppress the formation or migration of dislocation [53].

In general, there are many different types of dislocations. The models described here often assume misfit dislocations. Further, the interaction between dislocations, dislocation multiplication, and dislocation pinning plays a role [40], which can, for example, slow down their mobility [38]. A model including a dislocation multiplication term in the Mader and Light model was introduced by Dodson and Tsao [54] in 1987 and yields a differential equation for the strain relaxation. It applies to several experimental data sets (e.g., the Ge_xSi_{1-x}/Si system [53]). The interaction between dislocations was studied with computational models [55] and transmission electron microscopy provided experimental evidence of dislocations blocking each other's migration [56,57].

Freund (1990) introduced a theoretical model for strain relaxation taking into account the interaction of dislocations, to be precise the interaction of a threading dislocation and an interface misfit dislocation [58]. Slightly modified expressions of this model for the strain relaxation show a good agreement with in situ stress or strain

relaxation measurements [59,60]. These theoretical frameworks are in general referred to as Freund's blocking criterion and the strain relaxation is described as

$$\epsilon(h) \propto \frac{b}{h} \ln\left(\frac{\beta h}{b}\right) \tag{5.6}$$

where β represents the size of the dislocation core [58–60]. The value of β is generally unknown, for the $Si_{1-x}Ge_x$ system, values of 0.7–8 have been reported [59] with a value of $\beta \approx 1$ as a more commonly used value [61]. The proportionality factor in Eq. (5.6) contains geometrical parameters of specific dislocations and elastic constants of the film.

In the models described so far (Eq. 5.6), the rate-limiting step for strain relaxation is the migration of the dislocations. An additional limitation of the models is that a layer-by-layer growth (Frank-van der Merve growth mode, Fig. 5.3) was assumed which can only be expected in the case of small lattice mismatches (below ~1%) and good wettability. For complete wetting of the substrate, the sum of the surface energy of the epitaxial film and the interface energy must be smaller than the substrate surface energy. The surface stress and energy of the film can also influence the relaxation process, especially in thin films where the surface energy is not negligible [62–64]. For example, Cammarata *et al.* showed how the stress during the initial stage of the growth can be much smaller or even have the opposite sign as compared to the equilibrium stress [65] (e.g., by Matthews and Blakeslee [51]). Moreover, if the crystallographic surface orientation of the film does not correspond to a crystal plane characterized by low surface Gibbs free energy, a facetted surface may be favored, [40] often associated with an island-like growth mode.

The formation of islands (Stranski-Krastanov or Volmer-Weber growth mode, Fig. 5.3) can also be driven by strain since the roughening of the surface reduces the average film strain as islands are more free to expand or contract than a flat surface in the layer-by-layer growth mode. A strained island deforms the substrate lattice in its immediate surrounding which is why islands are known/expected to repel each other [66–70].

It has been observed that homogeneous nucleation of dislocations is far more unlikely than the heterogeneous nucleation at the surface, interface, or in the vicinity

Fig. 5.3 Growth modes. The three growth mode categories are schematically shown. The Frank-van der Merwe growth mode corresponds to a layer-by-layer (2D) growth and the Volmer-Weber to an island (3D) growth. The Stranski-Krastanov growth mode is a mixture of the 2D and 3D growth modes.

of an irregularity, such as a surface defect, a geometrical imperfection, or a "concentration of stress" between islands [38–40]. Consequently, the island growth mode aides the strain relaxation by facilitating the nucleation of dislocations. Edge dislocations can be injected at the boundaries between growing islands when they first coalesce and these dislocations can glide along the interface. If a dislocation line or half-loop nucleates, their migration can relieve stress as discussed above (Fig. 5.2). As a result, the Volmer-Weber growth mode typically leads to a relatively large density of dislocations [40]. The theoretical description of the strain relaxation becomes more complex through the formation of islands. Beresford, Lynch, and Chason (2003) introduced a model for strain relaxation where the rate-limiting step for the relaxation is the nucleation of dislocations (resulting from island formation), instead of the migration of dislocations [71]. For InGaAs/GaAs heteroepitaxy, for example, this model provides a better description of the strain evolution than the model proposed by Dodson and Tsao [71].

More specialized models for strain relaxation have been proposed to predict the critical thickness and describe the relaxation during the growth on vicinal surfaces, in graded layers or in multilayers [40]. It was further found experimentally that the dislocation density decreases inversely proportional to the film thickness. Once most of the strain has been relieved, the threading dislocations can react with each other causing annihilation or coalescence [40,72]. Dislocation lines can also move to the edge of the sample and disappear, but this is only relevant for small areas [40]. For example, dislocation free and completely relaxed Ge pillars of around 5 μm width can be obtained by depositing and post-annealing Ge on Si pillars separated by deep trenches [73].

5.3 In situ strain or stress observation techniques

5.3.1 Diffraction-based techniques

5.3.1.1 X-ray diffraction

X-ray diffraction (XRD) measurements are typically used to analyze thin film strain ex situ [36,74,75]. For a crystal lattice, the distances between adjacent crystallographic planes are in the range of few Angstroms, so X-rays are needed to see an interference (diffraction) pattern. In a crystal, X-rays are reflected at lattice planes which are labeled with Miller indices (*hkl*). The condition for constructive interference of beams reflected at an angle θ_{hkl} by lattice planes (*hkl*) that are d_{hkl} apart is the Bragg equation

$$2d_{hkl}sin\left(d_{hkl}\right)=n\lambda \tag{5.7}$$

with n being the order of diffraction. This is equivalent to the Laue equation, which states that the difference between the incoming and the outgoing wave vector $\vec{k}$ of the X-ray beam must be a reciprocal vector $\vec{G}$ from one lattice point to another. $\vec{G}$ must

therefore be a linear combination of the vectors $\vec{g}_{1,2,3}$ which span the reciprocal crystal lattice

$$\vec{k}_{in} - \vec{k}_{out} = \vec{G} = h\vec{g}_1 + k\vec{g}_2 + l\vec{g}_3 \tag{5.8}$$

Looking at elastic scattering only, $|\vec{k}_{in}| = |\vec{k}_{out}|$, the reciprocal lattice points $\vec{k}_{out}$ lie on a sphere with radius $\left|\vec{G}\right|$ (the Ewald sphere). Depending on the crystal symmetry, certain reflections may be forbidden and some reflections may be more intense than others (Fig. 5.4).

The most frequently employed geometry for thin film XRD is the symmetric $\omega/2\theta$ scan ($\omega = \theta$) detecting the diffraction from planes parallel to the sample surface. From the 2θ value of a reflection the out-of-plane lattice parameter, and thus the strain of the film, is calculated using the Bragg equation. The out-of-plane strain is related to the in-plane strain over the Poisson ratio ν (Eq. 5.1). Particularly suited for directly examining the in-plane lattice constant in epitaxial thin films is reciprocal space mapping (RSM), where an asymmetric reflection ($\omega \neq \theta$) is mapped by scanning a certain range in ω and 2θ in reciprocal space. From the exact ω and 2θ position of the reflection, the in-plane and out-of-plane lattice parameters are determined. For $\vec{G} = Q_X\vec{e}_1 + Q_Y\vec{e}_2 + Q_Z\vec{e}_3$ with unit vectors $\vec{e}_{1,2,3}$ and the X-ray beam in the xz-plane ($Q_Y = 0$),

$$Q_X = \left|\vec{k}\right|[\cos(\theta - \omega) - \cos(\theta + \omega)]$$

$$Q_Z = \left|\vec{k}\right|[\sin(\theta - \omega) + \sin(\theta + \omega)]$$

with $\left|\vec{k}\right| = \frac{2\pi}{\lambda}$,$\lambda$ being the wavelength of the X-ray beam (e.g., for CuK_α, $\lambda = 1.54056$ Å) [36,76].

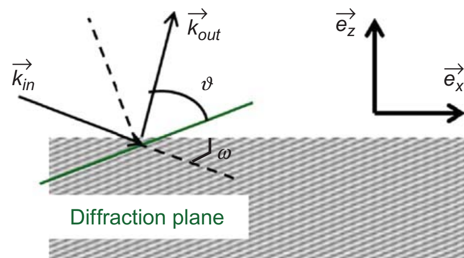

Fig. 5.4 Sketch of XRD on a lattice plane *(green)*. The angle of incidence with respect to the substrate surface is ω, θ is the angle of the reflected beam with respect to the lattice plane in question.

The issue with in situ online XRD measurements during film growth is that the measurements have to be fast enough to resolve the different growth stages. With a typical, lab-based thin film diffractometer, measurement of reciprocal space maps takes hours, a well resolved $\omega/2\theta$ scan of a few nm thick films take at least several minutes. Depending on the deposition rates, in several minutes the film may grow by many nm. As a consequence the thickness resolution of the strain evolution is low. To acquire fast enough measurements for monitoring the strain in situ, high intensity X-ray synchrotron based setups are required [76]. This raises the challenge of setting up a deposition facility to allow alignment of the sample with the beam. Further, the use of one-dimensional (1D) or two-dimensional (2D) detectors can reduce the measuring time. Depending on the type of XRD measurement is employed and on the deposition rate, the growth may be interrupted for a few *min* for each measurement [77,78]. Technical details for setting up a PLD chamber to conduct in situ synchrotron characterizations can be found elsewhere [79,80].

5.3.1.2 Reflection high-energy electron diffraction

Reflection high-energy electron diffraction (RHEED) is a well-established in situ monitoring technique [81] to observe the crystallinity and morphology of the surface of a growing film, allowing one to distinguish between the three growth modes. As the growth mode influences the film strain, RHEED is highly valuable in combination with any other in situ strain monitoring technique.

RHEED is a surface-sensitive grazing angle electron diffraction technique monitoring in situ the electron diffraction pattern generated at the surface of the sample under investigation. As for XRD, the Laue equation describes the diffraction condition. Owing to the high energy of the beam, ~30 keV, the radius of the Ewald sphere is much larger than the distance between reciprocal lattice points. The diffraction pattern corresponds to the intersection between the reciprocal lattice of the film and the Ewald sphere.

The atomically flat surface of a crystal is a two-dimensional lattice and consequently, the reciprocal lattice consists of rods extending out of the 2D plane of the crystal surface infinitely in the out-of-plane direction (Fig. 5.5). For any practical case the electron beam is not perfectly monochromatic and the variation in the electron energy broadens the Ewald's sphere shell, and the intersections with the lattice rods can be elongated vertically (streaks instead of dots). In the case of an island growth mode, however, the electron beam penetrates the islands and RHEED works in the so-called transmission mode, resulting in the diffraction pattern of a three-dimensional (3D) crystal (Fig. 5.5C). This is the same diffraction pattern as would be observed in transmission electron microscopy. More details can be found in textbooks dedicated to RHEED [81,82].

The diffraction pattern is made visible on a phosphors screen and is typically recorded with a CCD (charge coupled device) camera. The distance between diffraction spots or streaks is proportional to the in-plane reciprocal lattice parameter $q_{\text{in-plane}}$ as shown in Fig. 5.6. The conversion between relative spot distance and lattice parameter can be calibrated using the diffraction pattern of the substrate, whose lattice

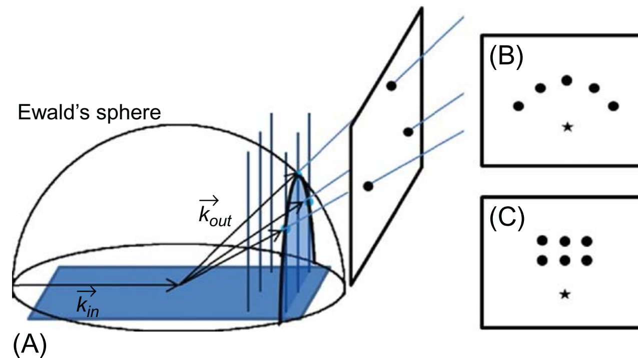

Fig. 5.5 Working principle of RHEED. Intersection of the Ewald sphere with lattice rods in reciprocal space (A). Resulting diffraction pattern of a flat surface (B) and a rough surface (C). A part of the direct beam may be visible *(star)*.

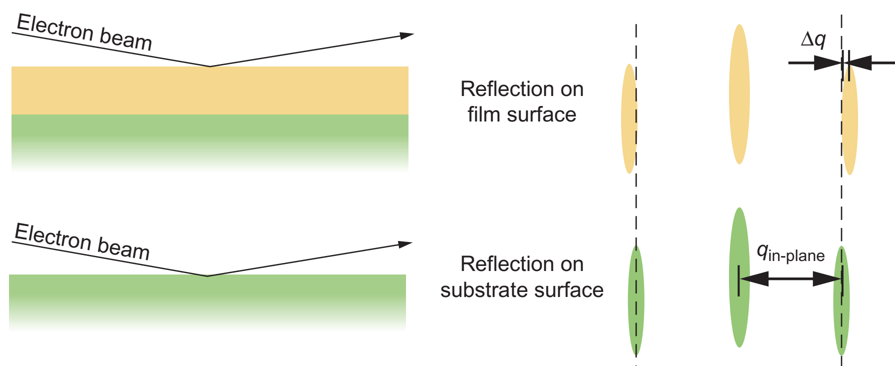

Fig. 5.6 In situ strain measurement by RHEED. The in-plane distance of the substrate reflections $q_{in\text{-}plane}$ is known.

parameter is well known. In a layer-by-layer growth mode, the in-plane lattice parameter of the film can be evaluated by measuring the variation of the relative distance between the diffraction spot of the RHEED pattern of the growing film.

The prerequisite for the strain analysis by RHEED is the resolution of the diffraction pattern which depends on the background pressure used during growth. The higher the deposition pressure, the larger the electron scattering cross section with the background gas leading to a broadening of the diffraction spots. The use of differentially pumped RHEED systems can alleviate this to some extent. In studies where RHEED was used to monitor the strain in situ in epitaxial metal oxide films, background pressures in the range of 10^{-6}–10^{-5} mbar were employed [60,83–85], while typical background pressures for the PLD were in the range between base pressure and 10^{-1} mbar [86,87].

5.3.2 Curvature-based techniques

Instead of obtaining the lattice distortion directly from the in-plane lattice parameter, the strain in a thin film can be characterized through the force the film exerts on the substrate, i.e., through the stress (see Section 5.1). As sketched in Fig. 5.7, a film under tensile strain leads to a contraction of the substrate surface and the induced radius of the curvature ρ is defined to be positive. For compressive strain the curvature is opposite and $\rho < 0$. Consequently, the film stress can be characterized *via* the substrate curvature.

In 1909 G.G. Stoney formulated the following equation, known as the Stoney formula [88], to correlate, under certain boundary conditions, the substrate curvature to the stress in a thin film of thickness h:

$$\frac{1}{\rho} = \frac{6(1-\nu)}{{h_s}^2 Y} h\sigma_f \tag{5.9}$$

where the thickness of the substrate $h_s \gg h$, with Y being the Young's modulus, and ν the Poisson ratio [37]. To compare the results from curvature-based and diffraction-based techniques, the elastic modulus E of the thin film must be known for converting strain to stress or *vice versa* (see Section 5.1). In some cases, strained thin films have elastic properties different to unstrained bulk [89] which may complicate the comparison. In other cases, the relation of strain measured by XRD to stress measured by curvature-based techniques works well with bulk elastic constants found in the literature [35].

For thin films growing on oxide substrates, the radii of curvatures induced by strain are typically of the order of kilometers, therefore a very sensitive technique is required to detect changes in ρ. To measure the change in curvature in situ, monitoring the variation of the deflection of one or more laser beams from the surface of the substrate yields the required sensitivity [37]. This technique is very sensitive to vibrations and requires a vibration-isolated environment. Typical vibration sources are vacuum pumps, or the target movement in the case of PLD [90]. Likewise small changes or fluctuations in the substrate temperature causes drifts in the measurements and the thermal expansion of the heater stage or the chamber are geometrical parameters

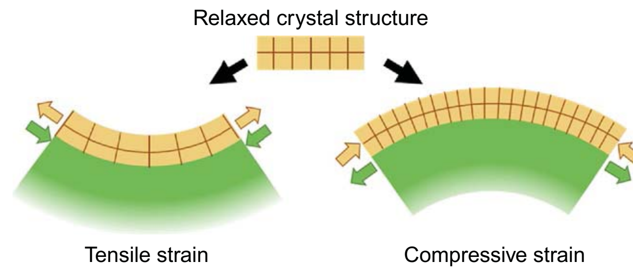

Fig. 5.7 Curvature-based stress measurement. An epitaxially strained film *(yellow)* exerts a force on the substrate surface *(green)* which makes the substrate bend. The radius of curvature and the lattice distortion in the film is exaggerated in this sketch to make the effect visible.

which can influence these curvature measurements greatly. Unlike conventional RHEED, the curvature-based stress monitoring is independent of the pressure of the background gas.

This kind of measurements requires flat substrate surfaces and chemically stable substrate materials. A substrate like $SrTiO_3$ is easy to reduce and loses oxygen at elevated temperatures. As a consequence, the detected changes in curvature for bare $SrTiO_{3.0}$ are determined by changes of the oxygen content in an oxygen-deficient $SrTiO_{3\text{-}\delta}$ layer with a different lattice constant than $SrTiO_{3.0}$. It was also found that in some cases, the oxygen content of a thin film grown on $SrTiO_3$ can largely originate from the substrate itself, as the oxygen uptake from the substrate is more effective than from the gaseous environment [91]. Obviously in these cases the substrate curvature cannot be related directly to the film stress. While $SrTiO_3$ is not suitable for multi-beam optical stress sensor (MOSS) measurements, other oxide substrates such as MgO, Al_2O_3, $LaAlO_3$, and $NdGaO_3$ are. In general, the measurement sensitivity of the growth stress in a specific material increases when using a more elastic substrate, since less energy is required to bend it.

The challenge when quantifying the strain with XRD or RHEED is to know the relaxed lattice constant. As mentioned earlier, small changes in the growth conditions can lead to a different composition including the oxygen composition and therefore a different lattice parameter. To ensure accuracy, either the film composition has to be verified or the relaxed lattice constant must be determined. A film is relaxed for certain if the in-plane and out-of-plane lattice constants are equal in RSMs, or if the in-plane lattice constant definitively has become constant with increasing thickness in RHEED measurements. The oxygen is more difficult to verify and is usually done ex situ using ion probe techniques [92]. A possible in situ approach is ellipsometry by monitoring the changes of the electronic states of the growing material. These changes in the electronic properties partly depend on the oxygen composition like in the case of $SrTiO_3$ or $CaCoO_{2.5+\delta}$ [93–95].

5.3.2.1 *Cantilever technique*

To measure the curvature, the substrate can be attached on one side only and viewed as a cantilever. The deflection of the cantilever can be measured with different methods [37]. Fig. 5.8 describes two different approaches: the deflection of a laser beam by the sample surface and a capacitive measurement. There is further possibility to measure the deflection force with a quartz microbalance [96]. As one side of the cantilever substrate is firmly fixed, clamping effects are an issue for this technique, but they can be reduced by using cantilevers with large length-to-width ratios [97].

For cantilever of length l, the deflection d is related to the radius of curvature $\rho = \frac{l^2}{2d}$, assuming $\rho \gg h_s$. Therefore, using Stoney's equation, the stress is related to d as follows [98]:

$$\sigma = \frac{Yh_s}{3l^2 h(1-\nu)} d \tag{5.10}$$

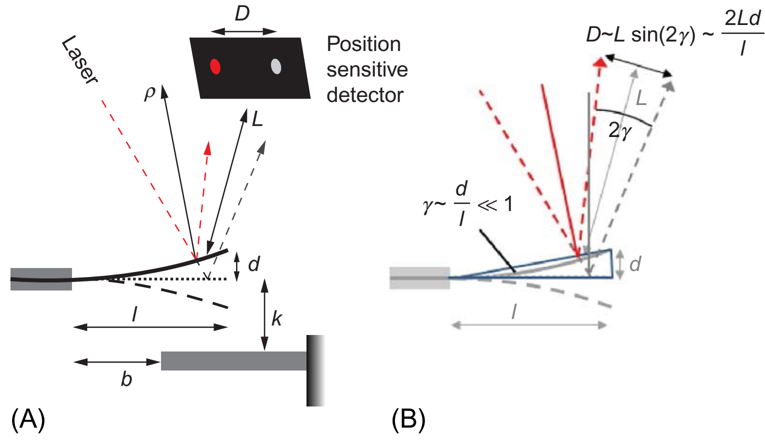

Fig. 5.8 Cantilever technique: The substrate = cantilever is fixed by clamping on one side; on the other it is free to bend (radius of curvature ρ). The bending is exaggerated for clarity; the *solid black line* is the case for tensile strain, the *dashed black line* for compressive strain and the *gray dashed line* for zero strain in (A). A change in the substrate curvature causes a displacement D of the laser spot on the detector or a change in capacitance (in relation to the *gray bar*) can be monitored. How the change in curvature affects the change in beam position D is sketched in (B).

To find d, a very small deflection is assumed so that $\rho \gg h_s$ and $\rho \gg l$. To monitor the change in curvature with a laser, the beam is reflected by the substrate and detected with a position-sensitive detector. When the film grows and the substrate bends, the movement of the reflected laser beam is monitored. From the substrate-detector distance L and the changes of the deflected beam position D (Fig. 5.8B), d is obtained as

$$d = \frac{Dl}{2L} \tag{5.11}$$

The deflection of the cantilever d can also be measured with capacitive methods[98]:

$$d = \frac{3w(l-b)l^2}{4\pi C^2(l^2 + bl + b^2)} \cdot \Delta C \tag{5.12}$$

Here w and l are the width and length of the cantilever, $C = (l-b)w/(4k\pi)$ the initial capacitance and ΔC is the change in capacitance due to the cantilever bending [98]. Since capacitive methods are not particularly suited for curvature monitoring in constrained space (e.g., in a deposition chamber), they are rarely used for in situ measurements during film growth [37].

5.3.2.2 Multi-beam optical stress sensor

The MOSS uses an array of parallel laser beams to map the changes in curvature of a surface in two dimensions. Instead of fixing the substrate on one side as in the cantilever method, here the substrate is free to bend thus avoiding clamping effects and restrictions to substrate size and shape. An example is shown in Fig. 5.9A, where a 10x10 mm^2 substrate is mounted on a sample holder and a 3x3 array of parallel laser beams is visible onto the substrate surface. The working principle is sketched in Fig. 5.9B and C. For simplicity two parallel laser beams are directed onto the substrate surface. As reference, the initial spacing D_0 between the laser spots is determined. During deposition the substrate curvature will changes and hence the distance D between the reflected spots.

From the mean differential spacing $(D-D_0)/D_0$, which is proportional to the curvature $1/\rho$ as defined by

$$\frac{1}{\rho} = -\frac{\cos\alpha}{2L} \cdot \frac{D-D_0}{D_0} \tag{5.13}$$

the film stress can be calculated using Stoney's equation (Eq. 5.8) with α, the angle of incidence and L, the distance between sample and CCD camera (see Fig. 5.9). The array of laser beams is created using two etalons. The position of the reflected laser beams is recorded with a CCD camera to evaluate the mean beam distances in the vertical and horizontal direction as a function of time. When using multiple beams, the average over all mean differential spacing values, horizontal or vertical, is taken.

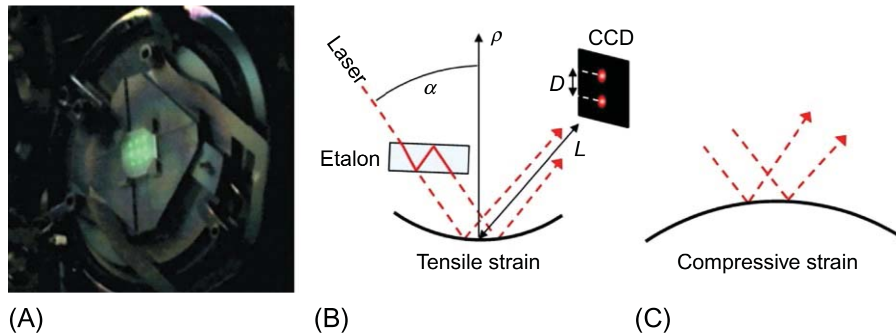

Fig. 5.9 Working principle of MOSS. (A) shows a 10×10 mm^2 substrate mounted free to bend. A 3×3 array of laser spots is visible on the surface. A laser beam is split into parallel beams with an etalon (B); for obtaining an $n \times m$ array, two etalons are used. For the sake of simplicity only two beams are shown here. The laser beams are reflected from the substrate surface toward a CCD camera that records their relative position and monitors the change of the relative distance among the laser spots, the distance between sample and CCD is L, the angle of incidence α. Depending on the radius of curvature ρ, D becomes smaller (tensile, (B)) or larger (compressive, (C)) during the film growth.

Optical techniques similar to MOSS scan one beam over the sample using a position-sensitive detector or a grid instead of an array of spots [37]. The advantage of the MOSS with respect to other optical curvature measurement techniques is that one can use almost any substrate, no position-sensitive detector is required and the noise is reduced by using multiple beams [37].

5.4 Application of in situ strain/stress monitoring techniques

5.4.1 X-ray diffraction

Structural distortion and domain formation in ferroelectric materials are expected to have a significant influence on their electric properties. To study the distortion and domain formation during the growth of $Ba_{0.5}Sr_{0.5}TiO_3$ on MgO at 750°C in detail, Bauer et al. (2014) employed in situ RSM at a synchrotron light source during the deposition using PLD [99]. Domains in $Ba_{0.5}Sr_{0.5}TiO_3$ are described as being shifted by half a unit cell along the *c*-axis with respect to each other but their formation is not fully understood yet. Since the average growth rate of 8.4 nm/min at 10 Hz is relatively fast, 1 min deposition and 10 min measurement sequences were alternated. The appearance of a second reflection in the RSM with different in-plane and out-of-plane lattice parameters at a thickness of ~140 nm is interpreted as the onset of domain formation [99].

Hur et al. (2004) characterized growth-induced strain during the growth of ZnO (0001) on Al_2O_3(0001) by symmetric out-of-plane measurements using synchrotron radiation [77]. The growth rate here was 0.6 nm/min, thus far slower as compared to the previous example. ZnO was deposited by RF (radio frequency) magnetron sputtering. During the initial stage, the film grows layer by layer and is fully strained. Above ~9 nm, the surface roughness increased strongly which correlated with the onset of relaxation.

Liang et al. (2005) prepared $BaTiO_3$/$LaNiO_3$ multilayers, each layer 3 nm thick, by sputtering on (001) $SrTiO_3$ [78]. After each bilayer, $\omega/2\theta$ scans were recorded in situ using synchrotron radiation. The first few bilayers were highly strained and the bilayer interfaces smooth. From the 10th bilayer onwards the growth front became rougher, the interface roughness increased as a result of interdiffusion and hence strain was released [78]. This is an example where interdiffusion between layers can reduce the strain.

5.4.2 Reflection-high energy electron diffraction

RHEED is the method with the largest number of in situ strain or stress studies for epitaxially grown oxide thin films. Bardal and coworkers (1994) studied the strain evolution by RHEED during the epitaxial growth of Y_2O_6-stabilized ZrO_2 (YSZ) on Si, which is used as buffer layers for the growth of high-temperature superconducting

films of $YBa_2Cu_3O_{7-x}$ [83]. The films were grown by e-beam evaporation in a background pressure of $5*10^{-6}$ mbar O_2 and the native amorphous silicon oxide layer was not etched away from the substrate surface. This native oxide layer reacts during growth with Y and Zr to form YSZ leaving volatile SiO. Below 7 nm YSZ, 0–0.5 nm silicon oxide remains at the interface. Above 5–7 nm the bulk lattice constant of YSZ is reached and the film grows elastically relaxed. Transmission electron microscopy showed that misfit dislocations at the interface accommodate the lattice mismatch. Niu and coworkers [100] using RHEED studied the growth of $SrTiO_3$ by MBE on Si in an oxygen partial pressure range of 10^{-6} mbar. $SrTiO_3$ grows initially in an amorphous phase but recrystallizes in a strained state. Increasing the thickness leads to plastic relaxation and the relaxed lattice parameter is reached at around 30 monolayers (~12 nm).

Merckling and coworkers (2007) used RHEED to study the strain relaxation in $LaAlO_3$ grown on $SrTiO_3$ by MBE in a background pressure of O_2 in the range of 10^{-6} mbar [84]. The in-plane lattice parameter of the film remains equal to that of the substrate in a layer-by-layer growth up to a critical thickness of 3.8 nm. This corresponds to ~3% tensile strain in the film. Above 3.8 nm the strain relaxes almost linearly with the increasing thickness up to ~12 nm. From thereon, the lattice parameter remains constant and is equal to the relaxed $LaAlO_3$ lattice parameter (see Fig. 5.10A).

Vassent and coworkers [60] investigated the strain relaxation of MgO grown on Fe(001). The growth mode and relaxation behavior were found to depend on temperature. The films were grown by MBE in the pressure range of 10^{-9} mbar and the lattice mismatch between film and substrate was -3.8%. It was found that the strain relaxes faster at higher temperatures. The strain relaxation was found to be slower than predicted by the Matthews and Blakeslee model but Freund's Blocking criterion could appropriately fit the data [60] (see Fig. 5.10B).

Peng and coworkers (2003) grew $SrTiO_3$ with 7.5% tensile mismatch on MgO and with −3% compressive mismatch on $LaAlO_3$ using reactive co-evaporation in the O_2 pressure range of 10^{-5} mbar [101]. The relaxation was analyzed at different deposition temperatures. At 830°C, the relaxation starts immediately (i.e., very small critical thickness) and at ~50 nm the films are fully relaxed (~0% strain) (see Fig. 5.10C). Most of the relaxation takes place during the first ~10 nm, i.e., there is a steep drop in strain. From thereon, the strain slowly approaches 0%. The strain relaxed much slower when the deposition temperature was reduced to 760°C and relaxation is reached at 250 nm. The high-temperature data is in agreement with theoretical predictions [101,103].

Zhu and coworkers (2008) studied the strain and the growth mode of $BaTiO_3$ and MgO grown by PLD on (001)-oriented $SrTiO_3$ at 10^{-8} mbar oxygen partial pressure [102]. The lattice mismatch between $BaTiO_3$ and $SrTiO_3$ is 2.2%, so that $BaTiO_3$ on $SrTiO_3$ grows in compressive strain (see Fig. 5.10D and E). The strain in the layer-by-layer grown $BaTiO_3$ relaxes rapidly after eight monolayers, in good agreement with the Matthews and Blakeslee model. The strain in MgO grown with ~8% mismatch on $SrTiO_3$ relaxes after the first monolayer and decreases almost linearly

with increasing thickness. The surface is initially flat but becomes rough and an island growth mode emerges within four monolayers. At ~10 monolayers, the film is relaxed. The strain relaxation in MgO as a function of thickness strongly disagrees with the Matthews and Blakeslee model which can be attributed to the change in growth mode.

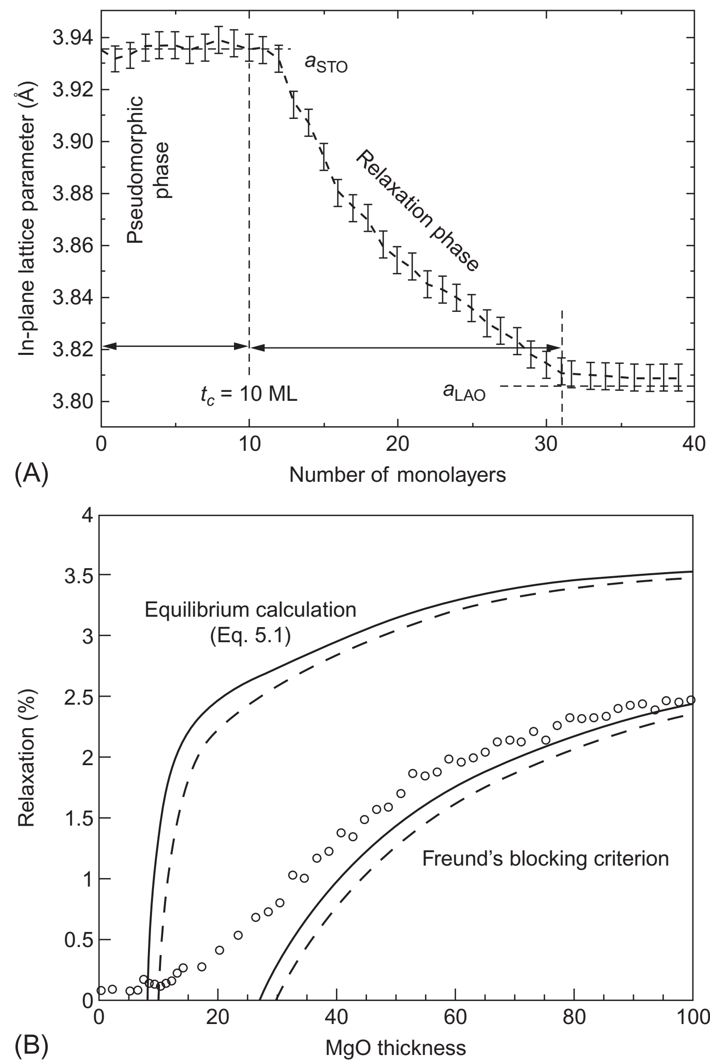

Fig. 5.10 Examples of strain relaxation data acquired with RHEED for epitaxial metal oxide thin films. (A) $LaAlO_3$ grown on $SrTiO_3$ [84]. (B) MgO on Fe, compared to the Matthews and Blakeslee model and Freund's blocking criterion [60].

(Continued)

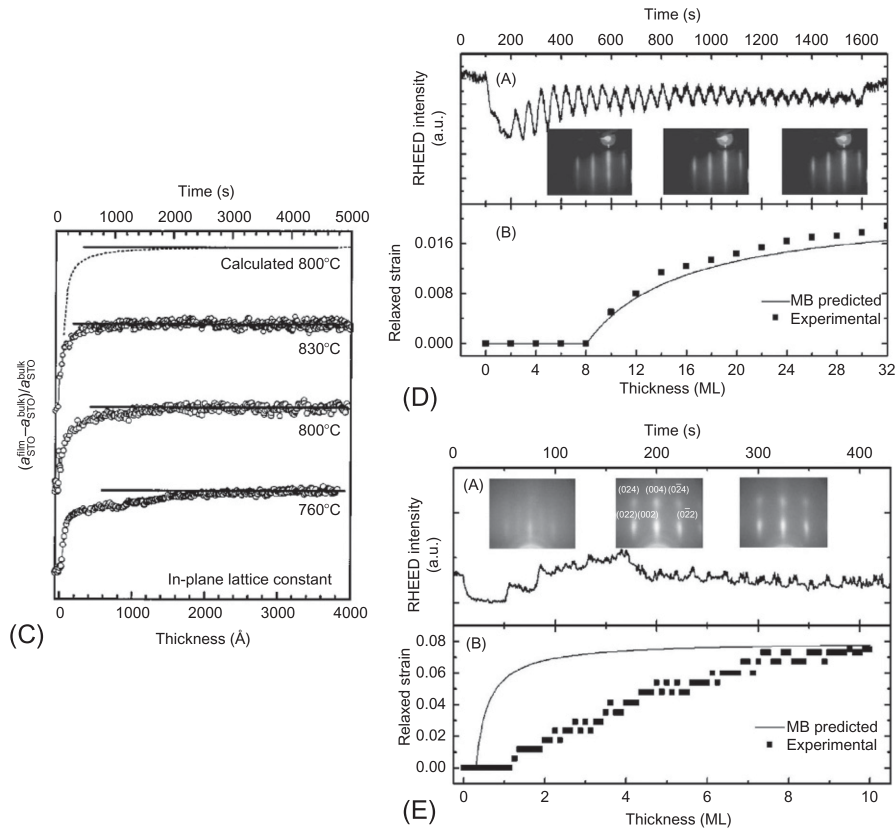

Fig. 5.10, Cont'd (C) $SrTiO_3$ grown on MgO at different temperatures, compared to the Matthews and Blakeslee model [101]. (D) $BaTiO_3$ and (E) MgO grown on $SrTiO_3$, the deviation in (D) from the Matthews and Blakeslee model is ascribed to the change in growth mode [102].

5.4.3 Cantilever technique

Early measurements (1969) of thin film stress with a cantilever technique made use of the change in capacitance to detect the deflection [98,104]. Likewise a quartz microbalance was used to measure the force that bends the substrate [96]. For oxides, this technique was mostly applied to characterize strain in polycrystalline films [105,106]. More recently, the cantilever technique was used to investigate the epitaxial growth of oxides. Premper and coworkers (2015) [107] studied the PLD growth of $SrTiO_3$ and $BaTiO_3$ on Pt single crystalline substrates. To reduce clamping effects a substrate of 12 mm × 2.5 mm × 0.1 mm ($l/w = 4$) is used. The in situ stress measurement was combined with simultaneous medium energy electron diffraction (MEED). The substrate is heated from the back with a radiative heater.

In a similar study, $SrTiO_3$ was grown on Pd single crystalline substrates ($f = -0.4\%$) by PLD in 10^{-4} mbar O_2 [90] and measured the strain with a two-beam configuration (see Fig. 5.11). For the first unit cell tensile stress was measured in spite of the compressive lattice mismatch. This is attributed to different bond formation in incomplete unit cell. Films with thickness of several unit cells show compressive stress in agreement with the lattice mismatch. Further it is shown that curvature-based stress measurements can have subunit cell thickness sensitivity (Fig. 5.11).

5.4.4 Multi-beam optical stress sensor

So far, the MOSS has mainly been used to study stress in epitaxially grown semiconductors [108–110] or in polycrystalline metal thin films [111–113]. As for the cantilever technique, studies on the growth of epitaxial oxide thin films are rare. Postdeposition studies have been done with the MOSS [114,115] on ceria thin films and also the growth of polycrystalline oxides was monitored [116,117].

The MOSS was used to study the stress in epitaxially growth Sm-doped ceria (SDC) [35]. Films were grown by PLD and the growth mode was simultaneously monitored by RHEED. The oxygen partial pressure required for the growth, $5*10^{-2}$ mbar was too high to use the RHEED pattern for strain analysis. For the MOSS measurements a 3×3 array of laser beams was used. Oxide single-crystal substrates (MgO,

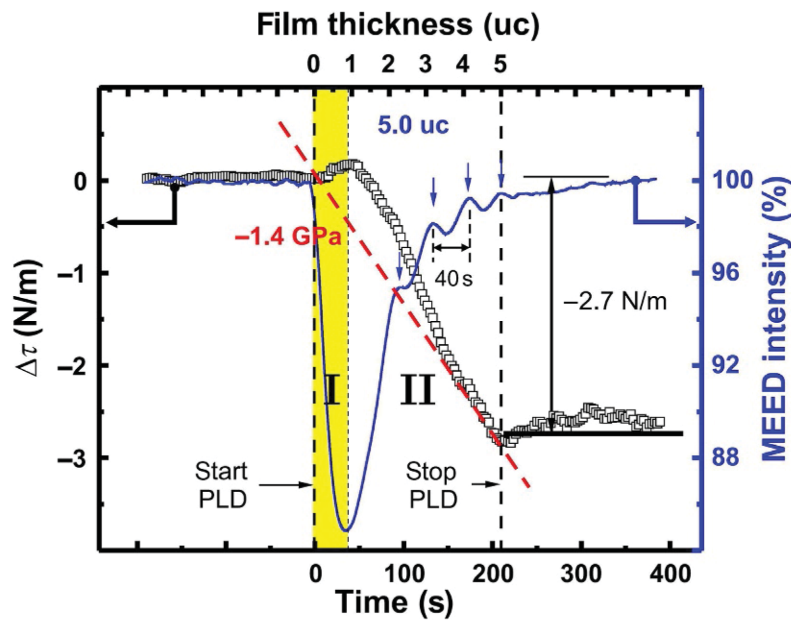

Fig. 5.11 Cantilever stress measurement of $SrTiO_3$ on (001)Pd [90]. The stress $\Delta\tau$ and the MEED intensity are shown as a function of time. The film thickness in unit cells is indicated during the growth.

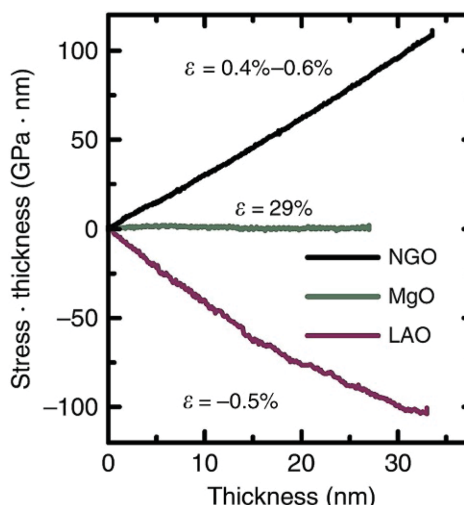

Fig. 5.12 MOSS measurement of SDC growth on (110)$NdGaO_3$ (NGO), (001) $LaAlO_3$ (LAO) and on (001)MgO substrates. Lattice mismatch values of film and substrate are indicated.

$NdGaO_3$, $LaAlO_3$) of $10 \times 10 \times 0.5$ mm^3 were used. A radiative heater was used, but oxide substrates do not absorb the heat similar to the metal cantilevers in the examples earlier. To ensure a sufficient heat transfer, the back of the substrate was Pt coated. This is necessary, since the MOSS sample holder only holds the substrate loosely at the corners so that it is free to bend (Fig. 5.9).

Comparing the growth on different single-crystal substrates, a roughly constant change in curvature, that is, a roughly constant stress was found for the total film thickness of ~30 nm. Ex situ RSM measurements showed that for mismatch values around ±0.5%, most of the mismatch was preserved. The difference between strain and lattice mismatch was likely due to the island growth mode. A large lattice mismatch between SDC (a = 5.43 Å) and MgO (a = 4.21 Å) was accommodated by introducing a high density of interface dislocations and the film grew epitaxially oriented but stress free (Fig. 5.12).

Similarly, the relaxation of the proton conductor Y-doped $BaZrO_3$ was studied. Here a buffer layer was used and the relaxation behavior for the film growth on the buffer layer is extremely similar to that in SDC in the study above. As a side remark, the MOSS can also be applied to monitor the thin film deposition in liquids, for example during the electrodeposition of ZrO_2 on Zr [118]. Van Overmeere and coworkers established the relationship between the curvature and the spot spacing for the case when the substrate is immersed in a liquid [118].

5.5 Summary and outlook

Without focussing on a specific class of materials, the presented techniques for in situ stress or strain characterization are well established. Most case studies of the epitaxial growth of metal oxides have been performed using diffraction-based techniques

(XRD, RHEED). These techniques provide a direct determination of the lattice distortion and further knowledge of materials properties such as elastic constants are not required. As a routine in situ technique to study strain, RHEED is restricted to lower background pressures than typically used for a metal-oxide deposition and XRD would require access to synchrotron radiation. While so far rarely used to study the epitaxial growth of metal oxides, optical techniques for stress measurements like curvature-based measurements or ellipsometry are therefore a good alternative and likely to gain wider use and acceptance in the future.

References

[1] D.K. Satapathy, et al., Phys. Rev. Lett. 108 (2012) 197201.
[2] J. Hoppler, et al., Nat. Mater. 8 (2009) 315.
[3] A. Ohtomo, H.Y. Hwang, Nature 427 (2004) 423.
[4] S. Thiel, G. Hammerl, A. Schmehl, C.W. Schneider, J. Mannhart, Science 313 (2006) 1942.
[5] A. Brinkman, et al., Nat. Mater. 6 (2007) 493.
[6] N. Reyren, et al., Science 317 (2007) 1196.
[7] A.D. Caviglia, M. Gabay, S. Gariglio, N. Reyren, C. Cancellieri, C. Cancellieri, Phys. Rev. Lett. 104 (2010) 126803.
[8] Y. Chen, N. Pryds, J.E. Kleibeuker, G. Koster, J. Sun, E. Stamate, B. Shen, G. Rijnders, S. Linderoth, Nano Lett. 11 (2011) 3774.
[9] F. Trier, et al., Phys. Rev. Lett. 117 (2016) 096804.
[10] A. Kalabukhov, R. Gunnarsson, J. Börjesson, E. Olsson, T. Claeson, D. Winkler, Phys. Rev. B 75 (2007) 121404.
[11] S. Thiel, C.W. Schneider, L.F. Kourkoutis, D.A. Muller, N. Reyren, A.D. Caviglia, S. Gariglio, J.M. Triscone, J. Mannhart, Phys. Rev. Lett. 102 (2009) 046809.
[12] S.A. Pauli, et al., Phys. Rev. Lett. 106 (2011) 036101.
[13] Y.Z. Chen, et al., Nat. Mater. 14 (2015) 801.
[14] A. Walsh, C.R.A. Catlow, K.H.L. Zhang, R.G. Egdell, Phys. Rev. B 83 (2011) 161202.
[15] F.Y. Bruno, et al., Phys. Rev. B 88 (2013) 195108.
[16] S. Li, X. Ding, J. Ren, X. Moya, J. Li, J. Sun, E.K.H. Salje, Sci. Rep. 4 (2014) 6375.
[17] R. Ramesh, N.A. Spaldin, Nat. Mater. 6 (2007) 21.
[18] C. Escorihuela-Sayalero, O. Diéguez, J. Íñiguez, Phys. Rev. Lett. 109 (2012) 247202.
[19] P. Strasser, et al., Nat. Chem. 2 (2010) 454.
[20] A. Llordés, et al., Nat. Mater. 11 (2012) 329.
[21] G. Giri, et al., Nature 480 (2011) 504.
[22] J.A. Kilner, Nat. Mater. 7 (2008) 838.
[23] B. Yildiz, MRS Bull. 39 (2014) 147.
[24] M. Mavrikakis, B. Hammer, J.K. Nørskov, Phys. Rev. Lett. 81 (1998) 2819.
[25] H. Wang, et al., Science 354 (2016) 1031.
[26] M. Escudero-Escribano, et al., Science 352 (2016) 73.
[27] V. Petkov, Y. Ren, S. Shan, J. Luo, C.-J. Zhong, Nanoscale 6 (2014) 532.
[28] B. Yildiz, MRS Bull. 10 (2014) 147.
[29] S.A. Akhade, J.R. Kitchin, J. Chem. Phys. 135 (2011) 104702.
[30] Z. Cai, Y. Kuru, J.W. Han, Y. Chen, B. Yildiz, J. Am. Chem. Soc. 133 (2011) 17696.

[31] S.E. Temmel, E. Fabbri, D. Pergolesi, T. Lippert, T.J. Schmidt, ACS Catal. 6 (2016) 7566.
[32] J.H. Haeni, et al., Nature 430 (2004) 758.
[33] K.J. Choi, et al., Science 306 (2004) 1005.
[34] K. Shimamoto, S. Mukherjee, N.S. Bingham, A.K. Suszka, T. Lippert, C. Niedermayer, C.W. Schneider, Phys. Rev. B 95 (2017) 184105.
[35] A. Fluri, D. Pergolesi, V. Roddatis, A. Wokaun, T. Lippert, Nat. Commun. 7 (2016) 10692.
[36] M. Birkholz, Thin Film Analysis by X-Ray Scattering, Wiley-VCH, Weinheim, 2006.
[37] L.B. Freund, S. Suresh, Film stress and substrate curvature, in: Thin Film Materials: Stress, Defect Formation and Surface Evolution, Cambridge University Press, 2004.
[38] M. Hanbücken, Stress And Strain In Epitaxy: Theoretical Concepts, Measurements and Applications, Elsevier, Amsterdam, 2001.
[39] U.W. Pohl, Epitaxy of Semiconductors: Introduction to Physical Principles, Graduate Texts in Physics, Springer Berlin Heidelberg, Berlin, Heidelberg, 2013.
[40] J.E. Ayers, Heteroepitaxy Of Semiconductors: Theory, Growth, and Characterization, CRC Press Taylor & Francis Group, Boca Raton, FL, 2007.
[41] C.M. Brooks, L.F. Kourkoutis, T. Heeg, J. Schubert, D.A. Muller, D.G. Schlom, Appl. Phys. Lett. 94 (2009) 162905.
[42] T. Ohnishi, K. Shibuya, T. Yamamoto, M. Lippmaa, J. Appl. Phys. 103 (2008) 103703.
[43] A. Ojeda-G-P, C.W. Schneider, M. Döbeli, T. Lippert, A. Wokaun, Appl. Surf. Sci. 389 (2016) 126.
[44] J. Chen, M. Döbeli, D. Stender, K. Conder, A. Wokaun, C.W. Schneider, T. Lippert, Appl. Phys. Lett. 105 (2014) 114104.
[45] S. Wicklein, A. Sambri, S. Amoruso, X. Wang, R. Bruzzese, A. Koehl, R. Dittmann, Appl. Phys. Lett. 101 (2012) 131601.
[46] C. Xu, S. Wicklein, A. Sambri, S. Amoruso, M. Moors, R. Dittmann, J. Phys. D. Appl. Phys. 47 (2014) 034009.
[47] I.V. Markov, Crystal Growth for Beginners, World Scientific, Singapore, 2003.
[48] S. Suresh, L.B. Freund, Thin Film Materials: Stress, Defect Formation and Surface Evolution, Cambridge University Press, Cambridge, 2006. Reprinted with corr. 2006 edn.
[49] F.C. Frank, J.H. van der Merwe, One-dimensional dislocations, II. Misfitting monolayers and oriented overgrowth, Proc. R. Soc. Lond. A Math. Phys. Sci. 198 (1949) 1053.
[50] J.W. Matthews, S. Mader, T.B. Light, J. Appl. Phys. 41 (1970) 3800.
[51] J.W. Matthews, A.E. Blakeslee, J. Cryst. Growth 27 (1974) 118.
[52] R. Hull, J. Bean, MRS Bull. 19 (1994) 32.
[53] J.C. Bean, L.C. Feldman, A.T. Fiory, S. Nakahara, I.K. Robinson, J. Vac. Sci. Technol. A 2 (1984) 436.
[54] B.W. Dodson, J.Y. Tsao, Appl. Phys. Lett. 51 (1987) 1325.
[55] K.W. Schwarz, J. Tersoff, Appl. Phys. Lett. 69 (1996) 1220.
[56] R. Hull, J.C. Bean, D.J. Eaglesham, J.M. Bonar, C. Buescher, Thin Solid Films 183 (1989) 117.
[57] E.A. Stach, R. Hull, R.M. Tromp, M.C. Reuter, M. Copel, F.K. LeGoues, J.C. Bean, J. Appl. Phys. 83 (1998) 1931.
[58] L.B. Freund, J. Appl. Phys. 68 (1990) 2073.
[59] V.T. Gillard, W.D. Nix, L.B. Freund, J. Appl. Phys. 76 (1994) 7280.
[60] J.L. Vassent, M. Dynna, A. Marty, B. Gilles, G. Patrat, J. Appl. Phys. 80 (1996) 5727.

[61] L.B. Freund, MRS Bull. 17 (1992) 52.
[62] R.C. Cammarata, Prog. Surf. Sci. 46 (1994) 1.
[63] H. Ibach, Surf. Sci. Rep. 29 (1997) 193.
[64] D. Sander, Curr. Opinion Solid State Mater. Sci. 7 (2003) 51.
[65] R.C. Cammarata, K. Sieradzki, F. Spaepen, J. Appl. Phys. 87 (2000) 1227.
[66] H.T. Johnson, L.B. Freund, J. Appl. Phys. 81 (1997) 6081.
[67] A.G. Cullis, MRS Bull. 21 (1996) 25.
[68] P.R. Markworth, X. Liu, J.Y. Dai, W. Fan, T.J. Marks, R.P.H. Chang, J. Mater. Res. 16 (2001) 2408.
[69] R. Kern, P. Müller, Surf. Sci. 392 (1997) 103.
[70] A. Tselev, R.K. Vasudevan, A.G. Gianfrancesco, L. Qiao, T.L. Meyer, H.N. Lee, M. D. Biegalski, A.P. Baddorf, S.V. Kalinin, Cryst. Growth Des. 16 (2016) 2708.
[71] R. Beresford, C. Lynch, E. Chason, J. Cryst. Growth 251 (2003) 106.
[72] R. Hull, J.C. Bean, Appl. Phys. Lett. 55 (1989) 1900.
[73] C.V. Falub, et al., Science 335 (2012) 1330.
[74] U. Pietsch, V. Holy, T. Baumbach, High-Resolution X-Ray Scattering: From Thin Films to Lateral Nanostructures, Springer, New York, 2013.
[75] D.K. Bowen, B.K. Tanner, High Resolution X-Ray Diffractometry and Topography, CRC Press, Boca Raton, FL, 2005.
[76] A.S. Brown, M. Losurdo, in: T.F. Kuech (Ed.), Handbook of Crystal Growth, second ed., North-Holland, Boston, MA, 2015, p. 1169.
[77] T.-B. Hur, Y.-H. Hwang, H.-K. Kim, H.-L. Park, J. Appl. Phys. 96 (2004) 1740.
[78] Y.C. Liang, H.Y. Lee, H.J. Liu, T.B. Wu, J. Cryst. Growth 276 (2005) 534.
[79] P.R. Willmott, et al., Appl. Surf. Sci. 247 (2005) 188.
[80] V. Vonk, S. Konings, L. Barthe, B. Gorges, H. Graafsma, J. Synchrotron Radiat. 12 (2005) 833.
[81] W. Braun, Applied RHEED: Reflection High-Energy Electron Diffraction During Crystal Growth, Springer Tracts in Modern Physics, 154, Springer, Berlin, 1999.
[82] A. Ichimiya, P.I. Cohen, Reflection High-Energy Electron Diffraction, Cambridge University Press, Cambridge, 2004.
[83] A. Bardal, T. Matthée, J. Wecker, K. Samwer, J. Appl. Phys. 75 (1994) 2902.
[84] C. Merckling, M. El-Kazzi, G. Delhaye, V. Favre-Nicolin, Y. Robach, M. Gendry, G. Grenet, G. Saint-Girons, G. Hollinger, J. Cryst. Growth 306 (2007) 47.
[85] C. Peng, J. Melnik, J. Li, J. Luo, A.R. Sanger, K.T. Chuang, J. Power Sources 190 (2009) 447.
[86] P.R. Willmott, J.R. Huber, Rev. Mod. Phys. 72 (2000) 315.
[87] D.B. Chrisey, G.K. Hubler, Pulsed Laser Deposition of Thin Films, Wiley, New York, Hoboken, 1994.
[88] G.G. Stoney, Proc. R. Soc. London, Ser. A 82 (1909) 172.
[89] A. Kossoy, E. Wachtel, I. Lubomirsky, J. Electroceram. 32 (2014) 47.
[90] J. Premper, D. Sander, J. Kirschner, Rev. Sci. Instrum. 86 (2015) 033902.
[91] C.W. Schneider, M. Esposito, I. Marozau, K. Conder, M. Doebeli, Y. Hu, M. Mallepell, A. Wokaun, T. Lippert, Appl. Phys. Lett. 97 (2010) 192107.
[92] M. Döbeli, J. Phys. Condens. Matter 20 (2008) 264010.
[93] J.H. Gruenewald, J. Nichols, S.S.A. Seo, Rev. Sci. Instrum. 84 (2013) 043902.
[94] W.S. Choi, H. Jeen, J.H. Lee, S.S.A. Seo, V.R. Cooper, K.M. Rabe, H.N. Lee, Phys. Rev. Lett. 111 (2013) 097401.
[95] X.D. Zhu, W. Si, X.X. Xi, Q. Jiang, Appl. Phys. Lett. 78 (2001) 460.
[96] E. Klokholm, Rev. Sci. Instrum. 40 (1969) 1054.

[97] K. Dahmen, S. Lehwald, H. Ibach, Surf. Sci. 446 (2000) 161.
[98] J.D. Wilcock, D.S. Campbell, Thin Solid Films 3 (1969) 3.
[99] S. Bauer, S. Lazarev, A. Molinari, A. Breitenstein, P. Leufke, R. Kruk, H. Hahn, T. Baumbach, J. Synchrotron Radiat. 21 (2014) 386.
[100] G. Niu, G. Saint-Girons, B. Vilquin, G. Delhaye, J.-L. Maurice, C. Botella, Y. Robach, G. Hollinger, Appl. Phys. Lett. 95 (2009) 062902.
[101] L.S.J. Peng, X.X. Xi, B.H. Moeckly, S.P. Alpay, Appl. Phys. Lett. 83 (2003) 4592.
[102] J. Zhu, X.H. Wei, Y. Zhang, Y.R. Li, J. Appl. Phys. 100 (2006) 104106.
[103] S.P. Alpay, A.L. Roytburd, J. Appl. Phys. 83 (1998) 4714.
[104] R. Koch, H. Leonhard, G. Thurner, R. Abermann, Rev. Sci. Instrum. 61 (1990) 3859.
[105] J. Hinze, K. Ellmer, J. Appl. Phys. 88 (2000) 2443.
[106] D.R. Clarke, Curr. Opinion Solid State Mater. Sci. 6 (2002) 237.
[107] J. Premper, D. Sander, J. Kirschner, Appl. Surf. Sci. 335 (2015) 44.
[108] J.A. Floro, E. Chason, Appl. Phys. Lett. 69 (1996) 3830.
[109] R.N. Jacobs, M. Jaime Vasquez, C.M. Lennon, C. Nozaki, L.A. Almeida, J. Pellegrino, J. Arias, C. Taylor, B. Wissman, J. Electron. Mater. 44 (2015) 3076.
[110] J.M. Ripalda, et al., Appl. Phys. Lett. 100 (2012) 012103.
[111] J.A. Floro, E. Chason, R.C. Cammarata, D.J. Srolovitz, MRS Bull. 27 (2002) 19.
[112] G. Abadias, L. Simonot, J.J. Colin, A. Michel, S. Camelio, D. Babonneau, Appl. Phys. Lett. 107 (2015) 183105.
[113] T. Scharf, J. Faupel, K. Sturm, H.-U. Krebs, J. Appl. Phys. 94 (2003) 4273.
[114] B.W. Sheldon, S. Mandowara, J. Rankin, Solid State Ionics 233 (2013) 38.
[115] B.W. Sheldon, J.D. Nicholas, S. Mandowara, J. Am. Ceram. Soc. 94 (2011) 209.
[116] S. Michotte, J. Proost, Sol. Energy Mater. Sol. Cells 98 (2012) 253.
[117] H.Y. Yeom, N. Popovich, E. Chason, D.C. Paine, Thin Solid Films 411 (2002) 17.
[118] Q. van Overmeere, J.F. van Humbeeck, J. Proost, Rev. Sci. Instrum. 81 (2010) 045106.